

Article

# Magnetic and Characterization Studies of CoO/Co<sub>3</sub>O<sub>4</sub> Nanocomposite

Ghadah M. Al-Senani <sup>1</sup>, Nasrallah M. Deraz <sup>2,\*</sup> and Omar H. Abd-Elkader <sup>3,4</sup>

<sup>1</sup> Department of Chemistry, College of Science, Princess Nourah Bint Abdulrahman University, 84428, Riyadh 11671, Saudi Arabia; gmalsnany@pnu.edu.sa

<sup>2</sup> Physical Chemistry Department, National Research Centre, Dokki, El Behooth St., Giza 12622, Egypt

<sup>3</sup> Physics and Astronomy Department, Science College, King Saud University, P.O. Box 2455, Riyadh 11451, Saudi Arabia; omabdelkader7@ksu.edu.sa

<sup>4</sup> Physics Division, Electron Microscope and Thin Films Department, National Research Centre, El Behooth St., Giza 12622, Egypt

\* Correspondence: nmderaz@yahoo.com

Received: 11 May 2020; Accepted: 13 July 2020; Published: 15 July 2020



**Abstract:** CoO/Co<sub>3</sub>O<sub>4</sub> nanoparticles (NPs) were synthesized by using a fresh egg white-assisted combustion method which acts as a new approach for green synthesis of this composite. This method was carried out by the direct heat of cobalt precursor with egg white at low temperature for very short period. In fact, this route is a novel, cheap and appropriate technique yielding nanoparticle-based materials. CoO/Co<sub>3</sub>O<sub>4</sub> nanoparticles were characterized by examining the structure and identifying the elements and determining the morphology via XRD, FTIR, SEM, EDS and TEM techniques. The sample magnetic observations were measured through the use of a vibrating sample magnetometer (VSM). The results of XRD, EDS, SEM and TEM confirmed the positive synthesis of the cubic CoO/Co<sub>3</sub>O<sub>4</sub> NPs with sponge crystals which proceed. For the as synthesized composite, 57.75 m<sup>2</sup>/g, 0.0148 cc/g and 10.31 nm were identified to be the  $S_{BET}$ ,  $V_p$  and  $\hat{r}$ , respectively. The cobalt oxide particles in their nature were polycrystalline, and the crystallite sizes varied from 10 to 20 nm. The magnetic measurement showed that the prepared nanocomposite displays room temperature ferromagnetism with an optimum value, 3.45 emu/g, of saturation magnetization.

**Keywords:** CoO/Co<sub>3</sub>O<sub>4</sub> NPs; XRD; SEM; TEM; EDS; VSM

## 1. Introduction

Solar energy is an important and vital source of energy because it is a renewable, inexpensive and infinite energy source. It constitutes an attractive source of energy for electrical, thermal and thermochemical applications [1]. In many countries of the world, solar energy may be absent for long periods, so thermal storage of solar energy has become a necessity. Therefore, thermal energy storage (TES) technologies were important and had a special place in the research process. More such technologies are regarded into three categories, based on sensitive, latent and thermochemical heat absorption and release [2]. Solar energy thermochemical storage systems (TCS) consist of reversible chemical reactions which absorb the solar heat during an endothermic step and release it through an exothermic reaction. TCS has the benefit of higher energy density stored (up to fifteen times greater than sensitive and six times greater than latent TES) [3]. Nevertheless, the energy storage density is one of the most significant factors of a TES system. CoO/Co<sub>3</sub>O<sub>4</sub> redox pairs have great potential as materials for high temperature solar energy storage [4]. For Mn<sub>2</sub>O<sub>3</sub>/Mn<sub>3</sub>O<sub>4</sub>, CuO/Cu<sub>2</sub>O and CoO/Co<sub>3</sub>O<sub>4</sub> the energy density was 202 kJ/kg, 811 kJ/kg and 844 kJ/kg, respectively [5].

Spinel Co<sub>3</sub>O<sub>4</sub> as a *p*-type semiconductor with various nano structural forms such as nano rods, nano sheets and ordered nano flowers has been synthesized [6–9]. Co<sub>3</sub>O<sub>4</sub>-based promising material

has been investigated with different applications such as catalysis processes, gas-sensing, solar energy absorption, magneto-electronics and electro chromic devices [10–14]. It may appear at first glance that the normal spinel structure of  $\text{Co}_3\text{O}_4$  is closely related to that of the inverse spinel  $\text{Fe}_3\text{O}_4$ . Nonetheless, compared to  $\text{Fe}_3\text{O}_4$ ,  $\text{Co}_3\text{O}_4$  exhibits strikingly different magnetic order. In particular,  $\text{Co}_3\text{O}_4$  does not exhibit ferrimagnetic ordering of the type demonstrated in  $\text{Fe}_3\text{O}_4$  since  $\text{Co}^{3+}$  ions are in low spin  $S = 0$  on octahedral B sites [15]. Alternatively, it demonstrates antiferromagnetic ordering on site A with each  $\text{Co}^{2+}$  ion requiring four adjacent  $\text{Co}^{2+}$  ions with reverses spins [16].

$\text{Co}_3\text{O}_4$  and CoO particles are generated largely by a broad range of wet chemical techniques such as spray-pyrolysis, freeze-drying, solubility-controlled synthesis, coprecipitation, combustion synthesis and sol-gel, [17–23]. To date, an information concerning synthesis of cobalt oxides varies with absence of studies on egg whites as fuel in preparation process of these oxides. In addition, knowledge of the egg-white-assisted green synthesis of cobalt oxides powders is scant. For this reason, the current work was confined to the synthesis of  $\text{CoO}/\text{Co}_3\text{O}_4$  NPs by using egg white which had not recently been reported in this reverence. Characterization and magnetic properties of the as synthesized nanocomposite were also decided.

## 2. Experimental

### 2.1. Materials

Cobalt (II) nitrate hexahydrate with linear formula  $\text{Co}(\text{NO}_3)_2 \cdot 6\text{H}_2\text{O}$  was the only chemical material and was supplied by Sigma-Aldrich Company. As this reagent was analytical grade, it was used without further cleansing. The egg white was extracted from local hens' fresh eggs.

### 2.2. Preparation Route

One sample of cobalt oxides was synthesized by mixing a detected weight of cobalt nitrate (2.91 g) with 5 mL of egg white, followed by continuous stirring at 80 °C in a Pyrex beaker that puted on hotplate to evaporate the water crystals, subsequently maximizing the viscosity of the resulting precursor sol as shown in Figure 1a. This sol was then heated at 120 °C to establish a gel (Figure 1b). The corresponding precursor gel was calcined for 15 min in a furnace at 350 °C, and then sparks appeared at one corner as shown in Figure 1c. These sparks spread across the entire prepared block, generating a good deal of foam which finishes by a black superfine massive powder (Figure 1d). Thus, the egg-white-assisted combustion method led to formation of a voluminous and flabby material containing porous cobalt oxides composite with a carbonaceous byproduct.

### 2.3. Characterization Techniques

A BRUKER D8 advance diffractometer (Bruker, Karlsruhe, Karlsruhe, Germany) used to measure the various mixed solids using an X-ray. The patterns were measured at 40 kV with  $\text{Cu K}_\alpha$  radiation and 40 mA, with a scanning speed of  $2^\circ \text{ min}^{-1}$  in  $2\theta$ . The crystallite sizes of  $\text{Co}_3\text{O}_4$  and CoO were defined by a broadening of the X-ray diffraction line using Scherrer equation [24].

$$d = B\lambda/\beta\cos\theta \quad (1)$$

where  $d$  is the examined process's average crystallite thickness,  $B$  is the Scherrer constant (0.89),  $\lambda$  is the X-ray wavelength,  $\beta$  is the diffraction's full-width half limit (FWHM) and  $\theta$  is the Bragg angle.

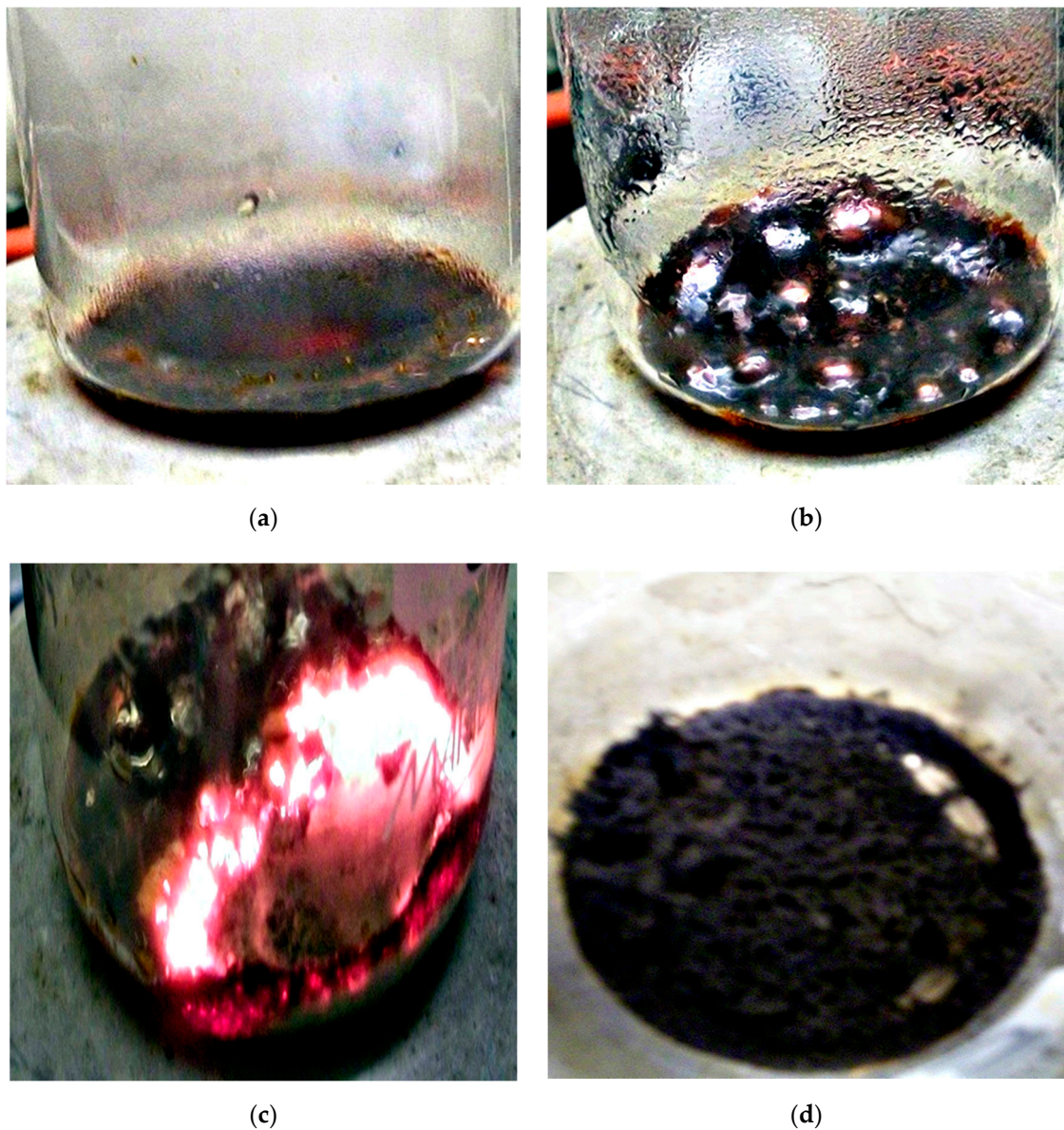


**Figure 1.** Process flowchart for fabricating the as-prepared sample: (a) precursor sol; (b) precursor gel; (c) flaming gel and (d) combusted product.

PerkinElmer Spectrophotometer (type 1430, Liantrisant, CF72 8YW, United Kingdom) was used to determine the Fourier-transform infrared spectrum (FTIR) of different solids. At wavelength from 4000 to  $400\text{ cm}^{-1}$  the spectra for IR were collected. Two mg of each solid sample were mixed with 200 mg of Potassium Bromide (KBr) grade vacuum-dried IR. Dispersed by grinding in a vibratory ball mill for 3 min, the mixture was inserted in a steel die 13 mm in diameter and exposed to a 12-ton strain. The sample discs were inserted in the double grating IR spectrometer holder.

A JEOL JAX-840A scanning electron microanalyzer (SEM) and JEOL Model 1230 (JEOL, Akishima, Tokyo, Japan) transmittance electron microanalyzer (TEM) captured the scanning and transmittance electron micrographs of the as-prepared solid, respectively. At first, the solid was washed in ethanol, and then ultrasonically adjusted to disperse individual particles over a small piece double-stick carbon tape putted over mount holders.

Energy dispersive X-ray analysis (EDS) was recorded on JEOL (JED-2200 Series) electron microscope with a Delta Kevex system attached (JEOL, Akishima, Tokyo, Japan).. The variables

were as follows: 15 kV voltage acceleration, 100 s time accumulation, 8  $\mu\text{m}$  width of window. The structure of surface molars was calculated by the Asa method, ZAF-correction, Gaussian extrapolation.

The surface properties of numerous solid catalysts—namely that surface basic area ( $S_{BET}$ ), total volume of pore ( $V_p$ ) and mean radius of pore ( $\hat{r}$ )—were calculated from isotherms measured at 77 K using a Nova 2000, Quanta Chrome (commercial BET unit, Boynton Beach, FL 33426, USA). Before undertaking these measurements, each sample was degassed for 2 h at 200 °C under a reduced pressure of  $10^{-5}$  Torr.

The magnetic features of the examined solids were measured in an optimum applied field of  $\pm 2000$  Oe at ambient temperature using a vibrating sample magnetometer (VSM; Lake Shore Model 7410, Weistron, West Hollywood, Hollywood, Los Angeles, CA, USA). A hysteresis loop acquired resulted in saturation magnetization ( $M_s$ ), remanence magnetization ( $M_r$ ), coercivity ( $H_c$ ) and squareness ( $M_r/M_s$ ) being calculated. The magnetic field was measured in the hysteresis loop with a relative error smaller than 0.0001%.

### 3. Results

#### 3.1. XRD Study

The XRD pattern of the as-synthesized CoO/Co<sub>3</sub>O<sub>4</sub> NPs is shown in Figure 2. The XRD trajectory demonstrates nanocomposite formation, which contained CoO and Co<sub>3</sub>O<sub>4</sub>. A series of diffraction peaks at degree  $2\theta = 31.19, 36.75, 38.25, 44.73, 55.47, 59.36, 65.37, 73.48, 76.67$  and  $77.7$  characteristic to indexing planes (220), (311), (222), (400), (422), (511), (440), (620), (533) and (622), respectively. These planes agree with the values reported for Co<sub>3</sub>O<sub>4</sub> NPs (PDF file No. 78-1970) [25]. In addition, these diffraction peaks can be indexed as typical cubic spinel structure for Co<sub>3</sub>O<sub>4</sub> (Major phase). Another series of diffraction peaks at degree  $2\theta = 36.37, 42.24, 61.28, 73.39$  and  $77.24$  characteristic to indexing planes (111), (200), (220), (311) and (222), respectively. These planes agree with the values reported for CoO NPs (PDF file No. 71-1187) [26]. However, these diffraction peaks can be indexed as typical cubic structure for CoO NPs. No other phases were observed in the XRD patterns. Moreover, in this study, one cannot ignore presence of a carbonaceous byproduct as impurities depended upon using egg white in the preparation method. This expectation will be confirmed in SEM and EDS sections.

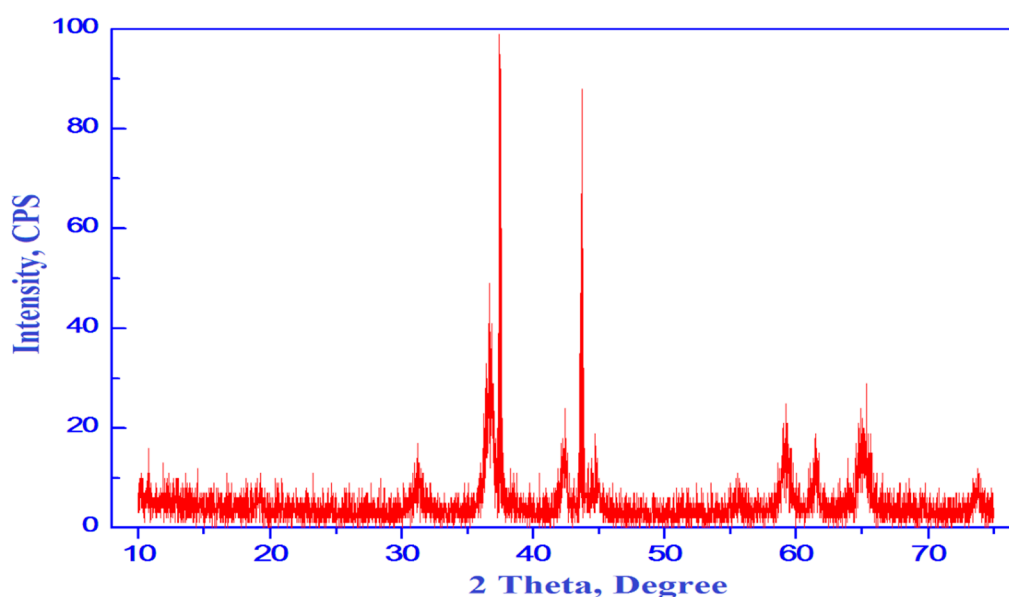


Figure 2. XRD pattern of CoO/Co<sub>3</sub>O<sub>4</sub> nanoparticles.

Thus, the XRD result displays the formation of CoO/Co<sub>3</sub>O<sub>4</sub> nanocomposite. Indeed, most of the peaks present in XRD pattern belong to Co<sub>3</sub>O<sub>4</sub> phase with fraction of cubic CoO. The height of the

diffraction peaks of  $\text{Co}_3\text{O}_4$  (311) and  $\text{CoO}$  (200) planes can be used for calculation of the relative content or the calculated fraction ( $F$ ) of  $\text{CoO}$  crystallites in the porous  $\text{CoO}/\text{Co}_3\text{O}_4$  nanocomposite depending upon the following relation:

$$F = I_{\text{cubic}}/I_{\text{total}} \quad (2)$$

where  $I_{\text{cubic}}$  is the count of  $I_{(200)}$  of cubic  $\text{CoO}$  phase and  $I_{\text{total}}$  is the sum of the counts of  $I_{(311)}$  and  $I_{(200)}$  for  $\text{Co}_3\text{O}_4$  and  $\text{CoO}$  phases, respectively. The fraction of cubic  $\text{CoO}$  phase present in porous  $\text{CoO}/\text{Co}_3\text{O}_4$  nanocomposite was found to be 32%. Depending on the calculations with fullprof program for Rietveld analysis (structure profile refinement) of X-ray powder diffraction data, the values of the crystallite size ( $d$ ), X-ray density ( $D$ ), unit cell volume ( $V$ ), lattice constants ( $a$ ) and dislocation density ( $\rho_d$ ) are tabulated in Table 1 [27].

**Table 1.** Structural properties of the as-synthesized cobalt oxides.

Properties	Values	
	$\text{Co}_3\text{O}_4$	$\text{CoO}$
Crystal structure	Cubic	Cubic
Lattice constant ( $a$ ), nm	0.8093	0.4267
Unit cell volume ( $V$ ), $\text{nm}^3$	0.5300	0.7770
Density ( $D$ ), $\text{g}/\text{cm}^3$	5.95	6.1
Dislocation density ( $\rho_d$ ), $\text{nm}^{-2}$	$4.444 \times 10^{-3}$	$6.944 \times 10^{-3}$
Crystallite size ( $d$ ), nm	15	12

The Miller indices,  $d$  spacing and the values of  $2\theta$  for the crystalline phases which present in the as-synthesized cobalt oxides are listed in Table 2.

**Table 2.** Miller indices,  $d$  spacing and the values of  $2\theta$  for the crystalline phases (cobalt oxides) in the as-synthesized solid.

$h$	$k$	$l$	$d$ spacing $\text{\AA}$	$2\theta$ (Obs.) Deg.	$2\theta$ (Cal.) Deg.	Differences	Phases
1	1	1	4.676	18.977	18.9935	-0.0165	$\text{Co}_3\text{O}_4$
0	2	2	2.860	31.267	31.2608	0.0062	$\text{Co}_3\text{O}_4$
1	1	1	2.463	36.47	36.4723	-0.0023	$\text{CoO}$
1	1	3	2.463	36.841	36.8346	0.0064	$\text{Co}_3\text{O}_4$
2	2	2	2.335	38.543	38.5356	0.0074	$\text{Co}_3\text{O}_4$
0	0	2	2.133	42.37	42.3656	0.0044	$\text{CoO}$
0	0	4	2.022	44.804	44.7954	0.0086	$\text{Co}_3\text{O}_4$
3	1	3	1.857	49.046	49.0665	-0.0205	$\text{Co}_3\text{O}_4$
2	2	4	1.651	55.647	55.6365	0.0105	$\text{Co}_3\text{O}_4$
1	1	5	1.557	59.348	59.3364	0.0116	$\text{Co}_3\text{O}_4$
0	2	2	1.508	61.47	61.4634	0.0066	$\text{CoO}$
0	4	4	1.430	65.225	65.2124	0.0126	$\text{Co}_3\text{O}_4$
1	3	5	1.367	68.618	68.604	0.014	$\text{Co}_3\text{O}_4$
2	4	4	1.348	69.731	69.7167	0.0143	$\text{Co}_3\text{O}_4$
1	1	3	1.286	73.63	73.6285	0.0015	$\text{CoO}$
2	0	6	1.279	74.109	74.0934	0.0156	$\text{Co}_3\text{O}_4$

### 3.2. FTIR Analysis

A spectrum FTIR of the as-prepared sample was shown in Figure 3. Examination of this figure indicated that: (i) this sample's spectra shows different bands at 3415, 1650, 1163, 643, 572 and 513  $\text{cm}^{-1}$ . These bands enabled us to identify of functional group and structure elucidation for the investigated samples; (ii) the observed wide bands belonging to the mixed oxides at 3415  $\text{cm}^{-1}$  and 1650  $\text{cm}^{-1}$  were due to the stretching and bending vibration of  $\text{H}_2\text{O}$  group OH [28]. However, the 1163  $\text{cm}^{-1}$  band can be correlated during the cooling process to the chemisorption's of  $\text{O}^{2-}$  on the sample surface particularly carbon surface; (iii) The spectra show a sharp 513- $\text{cm}^{-1}$  band with two 643- $\text{cm}^{-1}$  and 572

$\text{cm}^{-1}$  shoulder bands. These bands correspond to the  $\text{Co}_3\text{O}_4$  spinel structure [29]. It is understood that the characteristic bands of single and/or mixed oxides in the 1000 and  $400\text{ cm}^{-1}$  ranges are usually attributed to the vibration of metallic ions in the crystal lattice [29]. The spinel materials, however, are known to have two fundamental IR active modes in the vibration spectrum, which are high frequency bands around  $600\text{ cm}^{-1}$  at the tetrahedral (A) site and low frequency bands around  $400\text{ cm}^{-1}$  at octahedral (B) sites [30]. The bands in the obtained spectrum at  $513$  and  $643\text{ cm}^{-1}$  are correlated with vibrations of both the  $\text{Co}^{3+}$  in an octahedral hole and the  $\text{Co}^{2+}$  in a tetrahedral hole in the spinel lattice, respectively [31,32]. (iv) The divalent octahedral metal ion and oxygen ion complexes indicate the presence of the shoulder band at  $572\text{ cm}^{-1}$  [33]. In this analysis, the presence of some  $\text{Co}^{2+}$  ions at B-site could be due to this shoulder band.

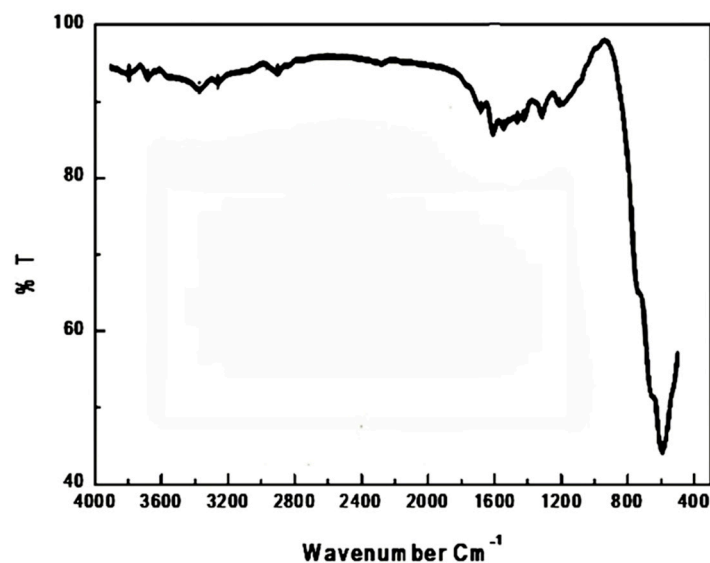


Figure 3. FTIR spectrum of  $\text{CoO}/\text{Co}_3\text{O}_4$  nanoparticles.

### 3.3. Energy Dispersive X-ray Spectrometry (EDS) Analysis

In order to confirm the existence of cobalt oxides and also to analyze the chemical structure and composition of the synthesized sample, EDS analysis was achieved. Illustration Figure 4 shows the EDS sequence of nanoparticles as synthesized. The characteristic signals of the elements of cobalt (Co), oxygen (O) and carbon (C) were calculated in Figure 4. Co: 76.7 wt percent, O: 20.2 wt percent and C: 3.1, respectively, were the weights percent of cobalt, oxygen and carbon measured from EDS. However, the value about 0.512 and 0.25 keV corresponds to the binding energies of oxygen ( $\text{O-K}_\alpha$ ) and ( $\text{C-K}_\alpha$ ), while the peaks at binding energies of 0.78, 6.92 and 7.68 keV correspond to  $\text{CoL}$ ,  $\text{CoK}_\alpha$  and  $\text{CoK}_\beta$ , respectively. This finding confirms that the as-prepared sample consisted entirely of mixed cobalt oxides and with a carbonaceous byproduct.

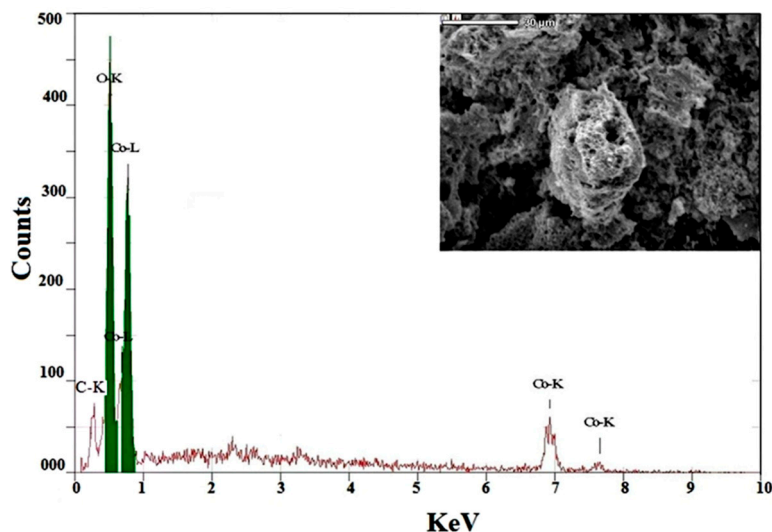
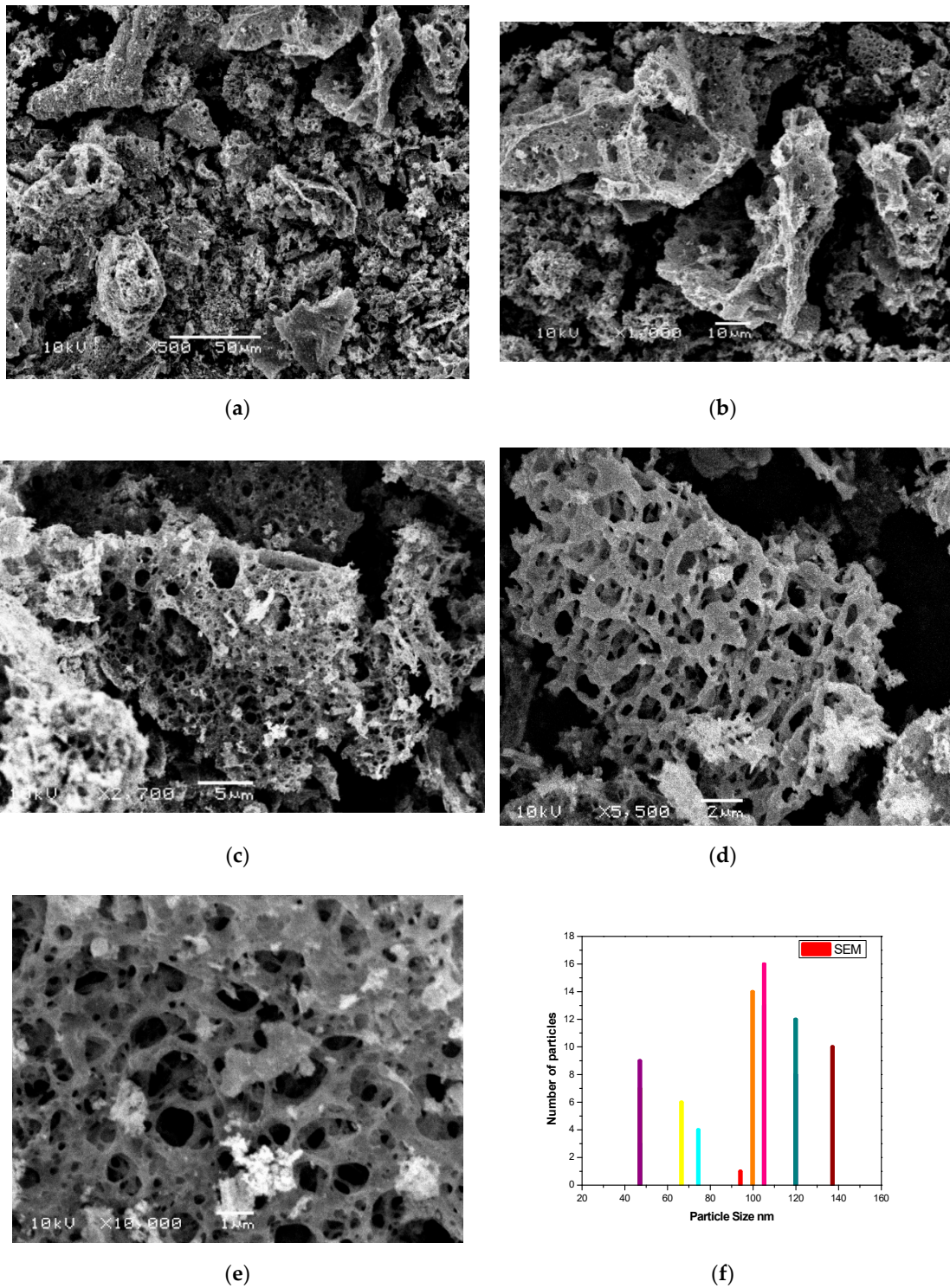


Figure 4. EDS pattern of CoO/Co<sub>3</sub>O<sub>4</sub> nanoparticles.

### 3.4. Morphologic Analysis

Scanning electron microscopic (SEM) analysis resulted in the surface morphology of the synthesized CoO/Co<sub>3</sub>O<sub>4</sub> nanoparticles. SEM images of the as-prepared nanoparticles with various magnifications are illustrated from Figure 5a–e. A higher tendency of agglomeration of many particles was observed. These agglomerations are gathered as sponge carrots. Such islands are like porous bodies with various types of pores and voids. Growth of the island was clearly seen from the tightly packed structures. Careful examination of SEM images indicates different contrast light of the as synthesized sample. Indeed, high contrast light nanoparticles, cobalt oxides, are clearly seen supported on a lower contrast darker porous material which is a carbonaceous byproduct. These features are also clearly visible in the lower magnification images. In addition, Figure 5f, there is histogram for particle size distribution of the as-prepared sample based on SEM micrographs [34]. This figure shows that the size of the as-prepared material was ranged between 10 and 140 nm with average sized located at 90 nm. This confirms formation of agglomerated particles in the as-prepared system.

Transmission electron microscopic (TEM) analysis has made a clear picture for morphologic characteristics of the as synthesized sample as shown in Figure 6a. Indeed, TEM enables data to be captured regarding the sample's inner structure, where SEM provides data about the surface of the analyzed object. However, this figure shows that the porous material (a carbonaceous byproduct with low contrast light) is mixed with high contrast light CoO/Co<sub>3</sub>O<sub>4</sub> nanoparticles. However, the synthesized material had homogenous structures and sizes ranged in the nanometer scale. In addition, Figure 6b, there is histogram for particle size distribution of the as-prepared sample based on TEM micrograph [34]. This figure confirms that the size of particle was in the range from 10 to 20 nm. Finally, these observations report the polycrystalline CoO/Co<sub>3</sub>O<sub>4</sub> NPs and also are consistent with XRD and EDS measurements.



**Figure 5.** (a–e) SEM images of the as-prepared sample with different magnifications and (f) its histogram for particle size distribution.

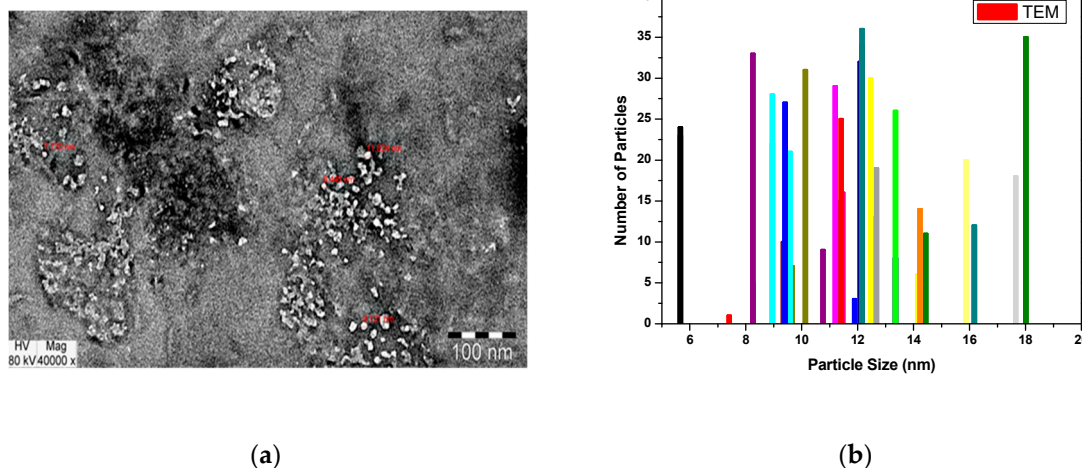


Figure 6. (a) TEM image of the as-prepared material and (b) its histogram for particle size distribution.

### 3.5. Surface Properties

Different surface properties were investigated from  $N_2$  adsorption isotherms conducted at 77 K, namely  $S_{BET}$ ,  $V_p$  and  $\hat{r}$ , for a synthesized composite. The  $S_{BET}$ ,  $V_p$  and  $\hat{r}$ , values were  $57.75 \text{ m}^2/\text{g}$ ,  $0.0148 \text{ cc/g}$  and  $10.31 \text{ nm}$ , respectively, for the as synthesized sample. These results confirm that the composite as-prepared is porous, with a powerful surface area depending upon presence of a carbonaceous byproduct and nature of the preparation method.

### 3.6. Magnetic Properties

A vibrating sample magnetometer (VSM) measured the magnetic properties of the  $\text{CoO}/\text{Co}_3\text{O}_4$  nanocrystals at room temperature. The magnetization plots ( $M_s$ ) as a function of the applied magnetic field ( $H$ ) are shown in Figure 7. This figure indicates a period of hysteresis estimated at 300 K. Table 3 includes  $M_s$ ,  $M_r$ ,  $H_c$  and  $M_r/M_s$  values of the as synthesized sample. The  $H_c$ ,  $M_s$  and  $M_r$  values were calculated as shown in literatures [35–37].

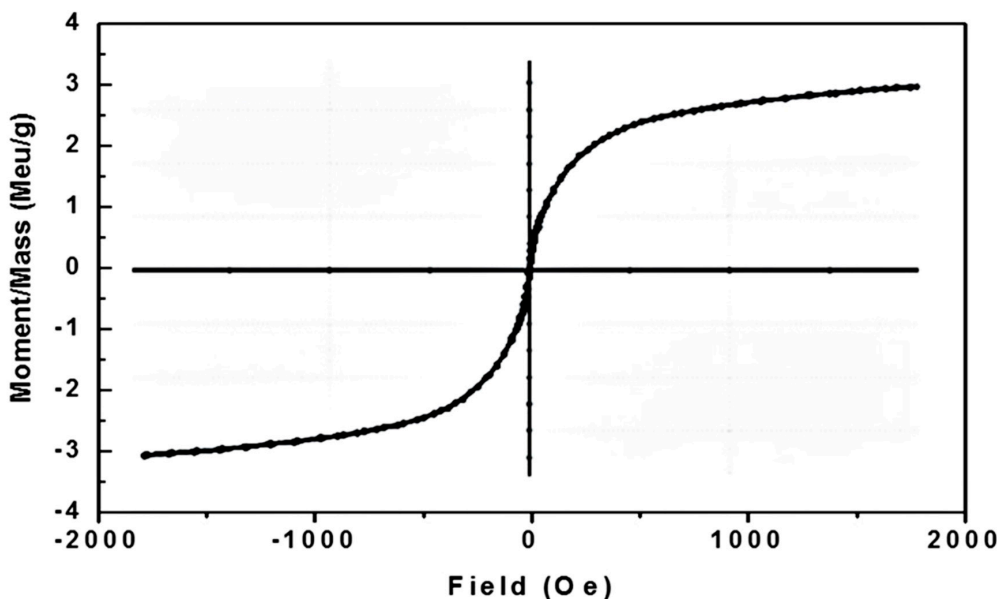


Figure 7.  $M$ - $H$  curve for  $\text{CoO}/\text{Co}_3\text{O}_4$  nanoparticles.

**Table 3.** Magnetic properties of the as-synthesized nanocomposite.

Properties	Values
Saturation magnetization ( $M_s$ ), emu/g	3.450
Remanent magnetization ( $M_r$ ), emu/g	0.2734
Coercivity ( $H_c$ ), Oe	85.032
Squareness ( $M_r/M_s$ )	$79.242 \times 10^{-3}$

#### 4. Discussion

There are three well-known valence states in the cobalt oxide system: cobalt oxide (CoO), cobalt oxide (Co<sub>2</sub>O<sub>3</sub>) and cobalt cobaltite (Co<sub>3</sub>O<sub>4</sub>). The most stable phase in this system is a mixed-valence compound with ordinary spinel structure [Co<sup>2+</sup>Co<sup>3+</sup><sub>2</sub>O<sub>4</sub>] [38]. In the current study, the egg-white-assisted green synthesis resulted in formation of nanocomposite containing CoO and Co<sub>3</sub>O<sub>4</sub>. The crystallite sizes of CoO/Co<sub>3</sub>O<sub>4</sub> mixed solids were ranged between 10 and 20 nm. The well-defined diffraction peaks involved in the spectrum of XRD indicate to formation of thin crystalline cubic phases. The preparation method led to formation fine size cobalt oxide powders depending upon on the peak broadening at each reflection. However, it can be seen from Table 1 that there was dislocation in the crystal lattice of CoO/Co<sub>3</sub>O<sub>4</sub> system. A crystallographic defect (irregularity) caused by the dislocation within a crystal structure that leads to changes in material properties. This fault distorts the ordinary atomic array of a perfect crystal [39–41].

A range of the synthesized CoO/Co<sub>3</sub>O<sub>4</sub> nanoparticles with overgrowth of clusters was observed in the SEM results. Spongy and fragile agglomerations with different pores and voids were observed. It was evident from the EDS spectrum that the CoO/Co<sub>3</sub>O<sub>4</sub> nanoparticles were synthesized successfully depending upon the major constituents of the as-prepared sample were Co and O elements with traces of carbon. In addition, the CoO/Co<sub>3</sub>O<sub>4</sub> composite consisted entirely of nanocrystalline particles based on the strong, intense, narrow width and sharp peaks involved in the EDS spectrum.

Table 3 reveals that the synthesized sample exhibits coercive magnetic hysteresis loops (85.032 Oe) and magnetization of saturation (3.45 emu/g). This indicates the ferromagnetism of the CoO/Co<sub>3</sub>O<sub>4</sub> NPs at room temperature. In other expressions, the behavior of the room temperature ferromagnetic (RTFM), as synthesized CoO/Co<sub>3</sub>O<sub>4</sub> NPs, showed very strong. Indeed, the efficient working of the spintronic devices relies on the semiconductor nanoparticles RTFM. Nonetheless, the origin of RTFM for the as synthesized CoO/Co<sub>3</sub>O<sub>4</sub> NPs, depending upon the presence of the unpaired electrons spin, could be attributed to the following reasons: (i) Surface uncompensated Co<sup>2+</sup> ions [42]; (ii) Range of the particles within nano scale [43]; (iii) Surface oxygen vacancies/or particle interface [44–48]; the oxygen vacancies in CoO/Co<sub>3</sub>O<sub>4</sub> nanoparticles were still a critical factor in the presence of RTFM. The oxygen vacancies play an important role in producing ferromagnetism especially in nanometric scale system. Opposite behavior was observed in a bulk system. This indicates the reduction of oxygen vacancies in the bulk system due to reduced oxygen vacancies density. To put it another way, ferromagnetism is inversely proportional to particle size. In nanosized materials, the loss of translational symmetry and weak surface coordination contribute to the occurrence of vacancies of oxygen with subsequent density increases. Furthermore, the oxygen vacancies are found primarily on the surface of the particles. Resultantly, it is assumed that these vacancies play a key role for the ferromagnetism identified in nanosized cobalt oxides. This could be due to trapping unpaired electrons in the oxygen vacancies and their spins will polarize together through interactions of exchange that create ferromagnetic order [49,50].

Additionally, one of the important unique properties which depend on its anisotropy is the squareness of a material. The squareness is also a function of the hysteresis loop forming the square. In the results of this study, CoO/Co<sub>3</sub>O<sub>4</sub> NPs, squareness was below 0.5. This result demonstrates that the particles interact by magnetostatic interaction, and anisotropy in the crystal lattice decreases [51–53]. However, it could explore the possibility of dealing with superparamagnetic particles in a blocked

state due to the small size of their nanocrystallites in the range of 10–20 nm [54]. In addition, cobalt nanoparticles provide a significantly greater anisotropy barrier elsewhere compared with average atomic thermal energy, and then the particle magnetization is stuck or “blocked” in a given direction until an external magnetic field reverses it. In other words, the possible mechanism for reduction of the squareness could be a direct consequence of the effect of the thermal fluctuations on change the direction of the magnetization for superparamagnetic particles. Similar results were observed in the case of spinel nickel manganites [55].

## 5. Conclusions

Green synthesis based on egg white brought about formation of CoO/Co<sub>3</sub>O<sub>4</sub> nanoparticles for the first time. This approach has many economic benefits for the synthesis of CoO/Co<sub>3</sub>O<sub>4</sub> nanoparticles without using any additives, such as technical feasibility, unexpectedness to scale up and less time consuming. From XRD results, the as synthesized material consisted entirely of CoO and Co<sub>3</sub>O<sub>4</sub> phases with cubic structure. The elemental and morphologic characteristics of the prepared sample were characterized using EDS and SEM techniques. The as-prepared CoO/Co<sub>3</sub>O<sub>4</sub> NPs have coercivity (85.032 Oe) and saturation magnetization (3.45 emu/g) with RTFM behavior.

**Author Contributions:** Conceptualization, N.M.D., G.M.A.-S. and O.H.A.-E.; methodology, N.M.D., G.M.A.-S. and O.H.A.-E.; software, O.H.A.-E.; validation, N.M.D., G.M.A.-S., and O.H.A.-E.; formal analysis, N.M.D. and O.H.A.-E.; investigation, N.M.D., G.M.A.-S. and O.H.A.-E.; resources, N.M.D., G.M.A.-S. and O.H.A.-E.; data curation, N.M.D., G.M.A.-S. and O.H.A.-E.; writing—original draft preparation, N.M.D., G.M.A.-S. and O.H.A.-E.; writing—review and editing, N.M.D., G.M.A.-S. and O.H.A.-E.; visualization, N.M.D., G.M.A.-S. and O.H.A.-E.; supervision, N.M.D., G.M.A.-S. and O.H.A.-E.; project administration N.M.D., G.M.A.-S.; funding acquisition, G.M.A.-S. All authors have read and agreed to the published version of the manuscript.

**Funding:** This research was funded by the Deanship of Scientific Research at Princes Nourah bint Abdulrahman University through the fast-track research-funding program.

**Conflicts of Interest:** The authors declare that they have no conflicts of interest.

## References

1. Romero, M.; Steinfeld, A. Concentrating solar thermal power and thermochemical fuels. *Energy Environ. Sci.* **2012**, *5*, 9234–9245. [CrossRef]
2. Aydin, D.; Casey, S.P.; Riffat, S. The latest advancements on thermochemical heat storage systems. *Renew. Sust. Energ. Rev.* **2015**, *41*, 356–367. [CrossRef]
3. Agrafiotis, C.; Roeb, M.; Sattler, C. Hybrid sensible/thermochemical solar energy storage concepts based on porous ceramic structures and redox pair oxides chemistry. *Energy Procedia* **2015**, *69*, 706–715. [CrossRef]
4. Agrafiotis, C.; Roeb, M.; Sattler, C. Exploitation of thermochemical cycles based on solid oxide redox systems for thermochemical storage of solar heat. *Sol. En.* **2014**, *102*, 189–211. [CrossRef]
5. Wong, B. *Thermochemical Heat Storage for Concentrated Solar Power*; U.S. Department of Energy. General Atomics Project 30314; 2011. Available online: <https://www.osti.gov/biblio/1039304> (accessed on 11 May 2020).
6. Gangopadhyay, S.; Hadjipanayis, G.C.; Sorensen, C.M.; Klabunde, K.J. Exchange anisotropy in oxide passivated Co fine particles. *J. Appl. Phys.* **1993**, *73*, 6964–6966. [CrossRef]
7. Resnick, D.A.; Gilmore, K.; Idzerda, Y.U.; Klem, M.T.; Allen, M.; Douglas, T.; Arenholz, E.; Young, M. Magnetic properties of Co<sub>3</sub>O<sub>4</sub> nanoparticles mineralized in *Listeria innocua* Dps. *J. Appl. Phys.* **2006**, *99*, 08Q501–08Q503. [CrossRef]
8. He, L.; Chen, C.; Wang, N.; Zhou, W.; Guo, L. Finite size effect on Néel temperature with Co<sub>3</sub>O<sub>4</sub> nanoparticles. *J. Appl. Phys.* **2007**, *102*, 103911–103914. [CrossRef]
9. Salabas, E.L.; Rumpelcker, A.; Kleitz, F.; Radu, F.; Schüth, F. Exchange anisotropy in nanocasted Co<sub>3</sub>O<sub>4</sub> nanowires. *Nano Lett.* **2006**, *6*, 2977–2981. [CrossRef]
10. Duan, X.; Huang, Y.; Agarwal, R.; Lieber, C.M. Single-nanowire electrically driven lasers. *Nature* **2003**, *421*, 241–245. [CrossRef]

11. Kim, H.; Park, D.W.; Woo, H.C.; Chung, J.S. Reduction of SO<sub>2</sub> by CO to elemental sulfur over Co<sub>3</sub>O<sub>4</sub>-TiO<sub>2</sub> catalysts. *Appl. Catal. B* **1998**, *19*, 233–243. [CrossRef]
12. Li, W.Y.; Xu, L.N.; Chen, J. Co<sub>3</sub>O<sub>4</sub> nanomaterials in lithium-ion batteries and gas sensors. *Adv. Funct. Mater.* **2005**, *15*, 851–857. [CrossRef]
13. Elliott, D.W.; Zhang, W.X. Field Assessment of Nanoscale Bimetallic Particles for Groundwater Treatment. *Environ. Sci. Technol.* **2001**, *35*, 4922–4926. [CrossRef] [PubMed]
14. O'Brien, S.; Brus, L.; Murray, C.B. Synthesis of Monodisperse Nanoparticles of Barium Titanate: Toward a Generalized Strategy of Oxide Nanoparticle Synthesis. *J. Am. Chem. Soc.* **2001**, *123*, 12085–12086. [CrossRef]
15. Roth, W.L. The magnetic structure of Co<sub>3</sub>O<sub>4</sub>. *J. Phys. Chem. Solids.* **1964**, *25*, 1–10. [CrossRef]
16. Dutta, P.; Seehra, M.S.; Thota, S.; Kumar, J. A comparative study of the magnetic properties of bulk and nanocrystalline Co<sub>3</sub>O<sub>4</sub>. *J. Phys. Condens Matter.* **2008**, *20*, 1–8. [CrossRef]
17. Zhao, Z.W.; Konstantinov, K.; Yuan, L.; Liu, H.K.; Dou, S.X. In-situ fabrication of nanostructured cobalt oxide powders by spray pyrolysis technique. *J. Nanosci. Nanotechnol.* **2004**, *8*, 861–866. [CrossRef]
18. Wu, J.G.; Tu, J.P.; Wang, X.L.; Zhang, W.K. Synthesis of nanoscale CoO particles and their effect on the positive electrodes of nickel–metal hydride batteries. *Int. J. Hydrog. Energy* **2007**, *32*, 606–610. [CrossRef]
19. He, T.; Chen, D.; Jiao, X.; Wang, Y.; Duan, Y. Solubility-controlled synthesis of high-quality Co<sub>3</sub>O<sub>4</sub> nanocrystals. *Chem. Mater.* **2005**, *17*, 4023–4030. [CrossRef]
20. Deraz, N.M. Catalytic decomposition of H<sub>2</sub>O<sub>2</sub> on promoted cobaltic oxide catalysts. *Mater. Lett.* **2002**, *57*, 914–920. [CrossRef]
21. Deraz, N.M. The Effect of Calcium Doping on the Surface and Catalytic Properties of Cobaltic Oxide Catalysts. *Adsorp. Sci. Technol.* **2003**, *21*, 229–243. [CrossRef]
22. Deraz, N.M.; Fouda, M.M.G. Fabrication and Magnetic Properties of Cobalt-Copper Nano-Composite. *Int. J. Electrochem. Sci.* **2013**, *8*, 2682–2690.
23. Toniolo, J.C.; Takimi, A.S.; Bergmann, C.P. Nanostructured cobalt oxides (Co<sub>3</sub>O<sub>4</sub> and CoO) and metallic Co powders synthesized by the solution combustion method. *Mater. Res. Bull.* **2010**, *45*, 672–676. [CrossRef]
24. Cullity, B.D. *Elements of X-ray Diffraction*; Addison-Wesley Publishing Co. Inc., Techpark: Singapore, 1976; Ch. 14.
25. Will, G.; Masciocchi, N.; Parrish, W.; Hart, M. Refinement of simple crystal structures from synchrotron radiation powder diffraction data. *J. Appl. Cryst.* **1987**, *20*, 394–401. [CrossRef]
26. Sasaki, S.; Fujino, K.; Takeuchi, Y. X-Ray Determination of Electron-Density Distributions in Oxides, MgO, MnO, CoO, and NiO, and Atomic Scattering Factors of their Constituent Atoms. *Proc Jpn. Acad* **1979**, *55*, 43–48. [CrossRef]
27. Boulton, A.; Louer, D. Powder pattern indexing with the dichotomy method. *J. Appl. Cryst.* **2004**, *37*, 724–731. [CrossRef]
28. Wang, Z.; Liu, Q.; Yu, J.; Wu, T.; Wang, G. Surface structure and catalytic behavior of silica-supported copper catalysts prepared by impregnation and sol–gel methods. *Appl. Catal. A-Gen.* **2003**, *239*, 87–94. [CrossRef]
29. Waldron, R.D. Infrared Spectra of Ferrites. *Phys. Rev.* **1955**, *99*, 1725–1727. [CrossRef]
30. Ouaguenouni, H.S.M.; Benadda, A.; Kiennemann, A.; Barama, A. Preparation and Catalytic Activity of Nickel–manganese oxide catalysts in the reaction of partial oxidation of methane. *Comptes Rendus Chim.* **2009**, *12*, 740–747. [CrossRef]
31. Liu, Y.; Zhu, G.; Ge, B.; Zhou, H.; Yuan, A.; Shen, X. Concave Co<sub>3</sub>O<sub>4</sub> octahedral mesocrystal: Polymer-mediated synthesis and sensing properties. *Cryst. Eng. Comm.* **2012**, *14*, 6264–6270. [CrossRef]
32. He, T.; Chen, D.; Jiao, X.; Xu, Y.; Gu, Y. Controlled Synthesis of Co<sub>3</sub>O<sub>4</sub> Nanoparticles through Oriented Aggregation. *Chem. Mater.* **2004**, *16*, 737–743. [CrossRef]
33. Berchmans, L.J.; Selvan, R.K.; Kumar, P.N.S.; Augustin, C.O. Structural and electrical properties of Ni<sub>1-x</sub>Mg<sub>x</sub>Fe<sub>2</sub>O<sub>4</sub> synthesized by citrate gel process. *J. Magn. Magn. Mater.* **2004**, *279*, 103–110. [CrossRef]
34. Rasband, W.S. *ImageJ*; U.S. National Institutes of Health: Bethesda, MD, USA, 1997–2012. Available online: <https://Imagej.nih.gov/ij/> (accessed on 11 May 2020).
35. Sandomirski, S. *Calculation and Analysis the Magnetic Parameters of the Minors Hysteresis Loop for Steels from the Basic Magnetic Parameters*. 19th World Conference on Non-Destructive Testing. 2016. Available online: [https://scholar.google.com.hk/scholar?hl=zh-TW&as\\_sdt=0%2C5&q=Calculation+and+Analysis+the+Magnetic+Parameters+of+the+Minors+Hysteresis+Loop+for+Steels+from+the+Basic+Magnetic+Parameters&btnG=](https://scholar.google.com.hk/scholar?hl=zh-TW&as_sdt=0%2C5&q=Calculation+and+Analysis+the+Magnetic+Parameters+of+the+Minors+Hysteresis+Loop+for+Steels+from+the+Basic+Magnetic+Parameters&btnG=) (accessed on 11 May 2020).

36. Sandomirski, S.G. The residual magnetization of the ferromagnetic body magnetized in an open magnetic circuit. *Defektoskopiia* **1997**, *8*, 50–59.
37. Sandomirski, S.G. Computing the Magnetization Curve and the Minors of the Hysteresis Loop for Structural Ferromagnetic Materials from the Basic Magnetic Parameters. *Elektrichestvo* **2010**, *1*, 61–64.
38. Shinde, V.R.; Mahadik, S.B.; Gujar, T.P.; Lokhande, C.D. Supercapacitive cobalt oxide (Co<sub>3</sub>O<sub>4</sub>) thin films by spray pyrolysis. *Appl. Surf. Sci.* **2006**, *252*, 7487–7492. [[CrossRef](#)]
39. Rendale, M.K.; Mathad, S.N.; Puri, V. Thick films of magnesium zinc ferrite with lithium substitution: Structural characteristics. *Int. J. Self-Propag. High-Temp. Synth.* **2015**, *24*, 78–82. [[CrossRef](#)]
40. Mathad, S.N.; Jadhav, R.N.; Patil, N.D.; Puri, V. Structural and mechanical properties of Sr<sup>2+</sup> doped bismuth manganite thick films. *Int. J. Self-Prop. High-Temp. Synth.* **2013**, *22*, 180–184. [[CrossRef](#)]
41. Mathad, S.N.; Jadhav, R.N.; Phadatare, V.; Puri, V. Structural and mechanical properties of Sr-doped barium niobate thick films. *Int. J. Self-Propag. High-Temp. Synth.* **2014**, *23*, 145–150. [[CrossRef](#)]
42. Xavier, S.; Thankachan, S.; Jacob, B.P.; Mohammed, E.M. Effect of Samarium Substitution on the Structural and Magnetic Properties of Nanocrystalline Cobalt Ferrite. *J. Nanosci.* **2013**, ID 524380, 1–7. [[CrossRef](#)]
43. Singh, J.; Chae, K. d<sup>0</sup> Ferromagnetism of Magnesium Oxide. *Condens. Matter* **2017**, *2*, 1–13.
44. Zou, G.F.; Li, H.; Zhang, D.W.; Xiong, K.; Dong, C.; Qian, Y.T. Well-aligned arrays of CuO nanoplatelets. *J. Phys. Chem. B* **2006**, *110*, 1632–1637. [[CrossRef](#)] [[PubMed](#)]
45. Xu, Q.; Gao, D.; Zhang, J.; Yang, Z.; Zhang, Z.; Rao, J.; Xue, D. Observation of room temperature ferromagnetism in pure La<sub>2</sub>O<sub>3</sub> nanoparticles. *Appl. Phys. A-Mater. Sci.* **2014**, *116*, 1293–1298. [[CrossRef](#)]
46. Kisan, B.; Alagarsamy, P. Room temperature ferromagnetism in finite sized ZnO nanoparticles. *Phys. B Condens. Matter* **2014**, *448*, 115–119. [[CrossRef](#)]
47. Shi, S.; Gao, D.; Xu, Q.; Yang, Z.; Xue, D. Singly-charged oxygen vacancy-induced ferromagnetism in mechanically milled SnO<sub>2</sub> powders. *RSC Adv.* **2014**, *4*, 45467–45472. [[CrossRef](#)]
48. Zhao, Y.; Zhao, J.Z.; Li, Y.L.; Ma, D.C.; Hou, S.N.; Li, L.Z.; Hao, X.L.; Wang, Z.C. Room Temperature Synthesis of 2D CuO Nanoleaves in Aqueous Solution. *Nanotechnology* **2011**, *22*, 115604–115613. [[CrossRef](#)]
49. Herzer, G. Nanocrystalline soft magnetic materials. *J. Magn. Mater.* **1992**, *112*, 258–262. [[CrossRef](#)]
50. Sharma, P.; Sharma, A. Structural and Magnetic Properties of Cobalt Oxide Nanoparticles at Different Annealing Temperatures. *Int. J. Mater. Sci. Eng.* **2016**, *4*, 208–214.
51. Razmara, Z. Synthesis, Characterization and Magnetic Properties of Bi-metallic Copper Complex, as a Precursor for the Preparation of CuO Nanoparticles and Its Application for Removal of Arsenic from Water. *J. Inorg. Org. Poly. Mater.* **2018**, *28*, 1255–1262. [[CrossRef](#)]
52. Zhu, D.Z.J.; Zhang, J.; Liu, T.; Chen, L.; Liu, X.; Ma, R.; Zhang, H.; Qiu, G. Controllable fabrication and magnetic properties of double-shell cobalt oxides hollow particles. *Sci. Rep.* **2015**, *5*, 8737.
53. NirmalleshNaveen, A.N. SubramanianSelladurai. Tailoring structural, optical and magnetic properties of spinel type cobalt oxide (Co<sub>3</sub>O<sub>4</sub>) by manganese doping. *Physica B* **2015**, *457*, 251–262.
54. Binns, C. *Introduction to Nanoscience and Nanotechnology*; John Wiley & Sons, Inc.: Hoboken, NJ, USA, 2010; p. 229.
55. Deraz, N.; Abd-Elkader, O.A.; Yassin, M. Impacts of Egg White Assisted Combustion and Ceramic Methods on Structural, Morphological and Magnetic Properties of Nickel Manganite System. *Crystals* **2020**, *10*, 489. [[CrossRef](#)]

